Research Article

π-electron weak ferromagnetism in potassium-intercalated 9-phenylanthracene

HPSTAR
1098-2021

Ming-An Fu [a, 1], Ren-Shu Wang [a, b, 1], Hui Yang [a], Pei-Yuan Zhang [a], Chun-Fang Zhang [c], Xiao-Jia Chen [b, **], Yun Gao [a, ***], Zhong-Bing Huang [a, *]

[a] Faculty of Physics and Electronic Technology, School of Materials Science and Engineering, Ministry-of-Education Key Laboratory for the Green Preparation and Application of Functional Materials, Hubei University, Wuhan, 430062, China
[b] Center for High Pressure Science and Technology Advanced Research, Shanghai, 201203, China
[c] College of Chemistry and Environmental Science, Hebei University, Baoding, Hebei, 071002, China

ARTICLE INFO

ABSTRACT

Intercalation of alkali metal is an effective way to tune the physicochemical property of polyaromatic hydrocarbons. Herein, we show for the first time that the weak ferromagnetism with a Curie temperature of 5.2 K can be realized in an all-carbon π-electron compound − potassium-intercalated 9-phenylanthracene. The magnetic measurements reveal that there exists an antiferromagnetic transition around 35 K before transition to the weak ferromagnetic phase. An in-depth theoretical investigation indicates that the weak ferromagnetism is produced by the intramolecular ferromagnetic and intermolecular antiferromagnetic spin couplings in the crystal unit cell. Our finding enriches the physical functionality of anthracene derivatives and adds a new member of organic magnetic materials.

© 2020 Elsevier Ltd. All rights reserved.

1. Introduction

Organic magnetic materials based on molecules [1], polymers [2−4], metal-organic frameworks [5−7] and carbon nanostructures [8−16] have been attracting great attention due to their potential applications in information storage and spintronics. It was found that vacancies or adatoms play a vital role in producing room temperature ferromagnetism in carbon nanostructures, including highly oriented pyrolytic graphite [8−11], polymerized fullerenes [12,13], and carbon nanotube [14,15]. As one large family of π-electron systems, polyaromatic hydrocarbons (PAHs) also found applications in magnetic materials besides their wide use in organic synthesis and catalysis. For instance, biphenyl was used as the spin coupler between two radicals, with either antiferromagnetic (AFM) or ferromagnetic (FM) coupling being induced, depending on the connection positions of radicals to biphenyl [17,18]. In one-dimensional vanadium-benzene sandwich clusters, the unpaired electron spins on the vanadium d_σ orbital couple ferromagnetically through the intervening benzene ligands [19]. Moreover, it was shown that introduction of carbon dangling bond into naphthalene under ultrasound treatment and low temperature annealing can produce room-temperature ferromagnetism in this simplest PAH [20]. Theoretical studies predicted that magnetic PAH molecules such as coronene and corannulene can be obtained by selectively hydrogenating their peripheral sites [21,22].

Recently, significant progresses have been made in searching for organic magnets via alkali reduction of PAHs. Two binary caesium salts of phenanthrene, $Cs(C_{14}H_{10})$ and $Cs_2(C_{14}H_{10})$, were synthesized by the reaction of Cs metal and phenanthrene in THF solution. The magnetic measurements showed that whereas $Cs_2(C_{14}H_{10})$ is diamagnetic owing to orbital polarization, $Cs(C_{14}H_{10})$ is a Heisenberg antiferromagnet with a gapped spin-liquid state emerging from the combination of low structural dimensionality and geometric spin frustration [23]. Similar quantum spin-liquid behavior was also observed in the potassium-reduced triphenylene compound $K_2(C_{18}H_{12})_2$(1,2-dimethoxyethane), in which strikingly strong AFM coupling exists between nearest neighbor S = 1/2 spins of $(C18H12)^{\cdot-}$ radical anions [24]. Using mixed-metal reduction of bowl-shaped corannulene, Spisak et al. synthesized a

---

* Corresponding author.
** Corresponding author.
*** Corresponding author.
  E-mail addresses: xjchen@hpstar.ac.cn (X.-J. Chen), gaoyun@hubu.edu.cn (Y. Gao), huangzb@hubu.edu.cn (Z.-B. Huang).
[1] Ming-An Fu and Ren-Shu Wang contributed equally to this work.

heterometallic sandwich-type aggregate, $[Cs^+//(C_{20}H_{10}^{3-})4K^+/(C_{20}H_{10}^{3-})//Cs^+]$ [25]. The diamagnetic ground state of the new heterometallic product indicates a weak AFM interaction between two trianion radicals through the potassium belt in the sandwich. They argued that the downsizing of the sandwiched alkali metals belts could tune the coupling of radicals from AFM to FM in nature [25].

Inspired by the above findings, we explore the magnetic property of potassium-intercalated 9-phenylanthracene (K-intercalated 9-PAN), one of the derivatives of anthracene, which have been widely used as organic light-emitting diodes [26], organic field-effect transistors and organic photovolatic devices [27]. In each 9-PAN molecule, one phenyl is connected to the 9-position of anthracene. Here, we show that when potassium atoms are intercalated into the crystal of 9-PAN, the newly synthesized materials exhibit AFM and FM transitions at 35 and 5.2 K, respectively. Theoretical calculations reveal that the magnetism of K-intercalated 9-PAN is determined by combining the FM and AFM couplings of unpaired electron spins on phenyl and anthracene anions, which are formed through transferring electron from potassium to carbon atom.

2. Experiments

2.1. Material synthesis

High-purity potassium metal (99% purity, Sinopharm Chemical Reagent) was cut into small pieces and mixed with 9-PAN (>98% purity, Tokyo Chemical Industry) with a nominal mole ratio of 3:1 in a glove box with the oxygen and moisture levels less than 0.1 ppm. The mixtures were then loaded into quartz tubes and sealed under a vacuum about 1×10^{-4} Pa. The sample tubes were treated in an ultrasound device at 75 °C for 10 h. After ultrasound treatment, the samples tubes were heated at 150 °C for two days.

2.2. Material characterization

In each experimental run, some powder from the same tube was put into a nonmagnetic capsule, a capillary and a mylar film covering sample cell, for the measurements of magnetization, Raman scattering and X-ray diffraction (XRD), respectively. The magnetization measurement was performed in a SQUID magnetometer (Quantum Design MPMS3) in the temperature range of 1.8–300 K. The crystal structures of pristine and potassium-intercalated samples were examined with an XRD diffractometer (Bruker D8 Advance). Chemical bonding and charge transfer process were analyzed using a Raman Spectrometer (LabRAM HR Evolution) that operated with a 633 nm laser of low power under 1 mW.

2.3. Theoretical calculations

The crystal and electronic structures of K-intercalated 9-PAN were calculated by the plane-wave pseudopotential method as implemented in the Vienna ab initio simulation package (VASP) [28,29]. The generalized gradient approximation (GGA) with Perdew-Burke-Ernzerhof (PBE) formula [30] for the exchange-correlation potentials and the projector-augmented wave method (PAW) [31] for ionic potential were used to model the electron-electron and electron-ion interactions. Plane wave basis sets with an energy cutoff of 450 eV and $3 \times 3 \times 3$ Monkhorst-Pack k-points mesh were adopted for geometry optimization. A finer $5 \times 5 \times 5$ k-point sampling scheme was used for calculating partial density of states (PDOS). The convergence criteria for the energy and max force are set to 10^{-4} eV and 0.01 eV/Å, respectively. The Raman

active modes for single 9-PAN molecule were calculated based on the density functional theory as implemented in Gaussian 09, revision D.01 [32], and the functional M06–2X with Def2TZVPP basis set was employed in the present work.

3. Results and discussion

3.1. Magnetic property of K-intercalated 9-PAN

Purchased 9-PAN exhibits a small and weak temperature-dependent *dc* magnetic susceptibility χ in the temperature range of 1.8–300 K (see Figure S1 in the Supplementary Data), demonstrating that there is no magnetic impurity in the non-intercalated material. Upon intercalating potassium into 9-PAN, all synthesized samples exhibit a clear FM transition at 5.2 K. The magnetic results for one representative sample (labeled as A) are summarized in Fig. 1. Fig. 1a shows χ in the applied magnetic fields of 20, 100, and 1000 Oe with field cooling (FC) and zero-field cooling (ZFC) in the temperature range of 1.8–50 K. Both FC and ZFC magnetic susceptibilities slowly increase with lowering temperature until 5.2 K, where a sudden increase of χ on cooling further signals a FM transition. The inset of Fig. 1a shows the temperature dependence of the ZFC magnetic susceptibility at 20 Oe in the region of 1.8–300 K. The data between 35 and 300 K can be well fitted by the Curie-Weiss law ($\chi = C/(T-\theta)$), with $C = 1.8 \times 10^{-4}$ emu·K·Oe^{-1}·g^{-1} and $\theta = -35.1$ K. The negative θ indicates that there exist dominant AFM interactions between unpaired electron spins. Fig. 1b displays the magnified FC and ZFC magnetic susceptibilities at 20 and 100 Oe in the region of 1.8–50 K. With decreasing temperature, χ deviates the Curie-Weiss behavior around 35 K and meanwhile a bifurcation appears between FC and ZFC curves, suggesting the development of magnetic ordering. The slow increase of ZFC χ below 35 K and its flattening near 10 K indicate a development of AFM order before phase transition to the FM state. A similar evolution of χ with lowering temperature was observed in CuF$_2$(-H$_2$O)$_2$(pyrazine), where the AFM and FM orderings develop at 10.5 and 4.3 K, respectively [33].

In Fig. 1c, we plot ZFC χT as a function of temperature in the region of 1.8–10 K. One can clearly see that in the applied magnetic field of 20 Oe, χT decreases continuously with lowering temperature and reaches a minimum of 3.4×10^{-5} emu·K·Oe^{-1}·g^{-1} at 5.2 K, below which χT turns to increase and reaches a maximum of 5.7×10^{-5} emu·K·Oe^{-1}·g^{-1} at 2.8 K, followed by a decrease until 1.8 K. As the magnetic field is increased to 100 Oe, the minimum and maximum shift to 4.8 and 3.4 K, respectively, accompanying a strong suppression of the hump structure. Further increasing of the magnetic field to 1000 Oe results in a continuous decrease of χT between 1.8 and 10 K. Such a strong magnetic field dependence of χT and its temperature evolution are consistent with the findings for several weak ferromagnets (canted antiferromagnets) [33–42]. Thus, the transition at 5.2 K observed in our samples corresponds to a weak FM type. Similar to other weak ferromagnets, the small spontaneous magnetization leads to a decrease of magnetic susceptibility with increasing magnetic field, as shown in Fig. 1a.

Further evidence for the existence of weak ferromagnetism in K-intercalated 9-PAN is presented in Fig. 1d, showing the M − H curves at 1.8 and 50 K in the region of −0.8-0.8 KOe. A linear dependence of M on H at 50 K just reflects the paramagnetic character before magnetic ordering. At the lowest accessible temperature of 1.8 K, a clear magnetic hysteresis appears in the M − H curve, and the coercivity (H$_c$) and remanent magnetization (M$_r$) are about 50 Oe and 0.8×10^{-3} emu·g^{-1}. Notice that beyond the magnetic fields of −558 Oe and +411 Oe, where the magnetic hysteresis loop closes, M still keeps a linear dependence on H and does not tend to reach saturation at high magnetic fields. This
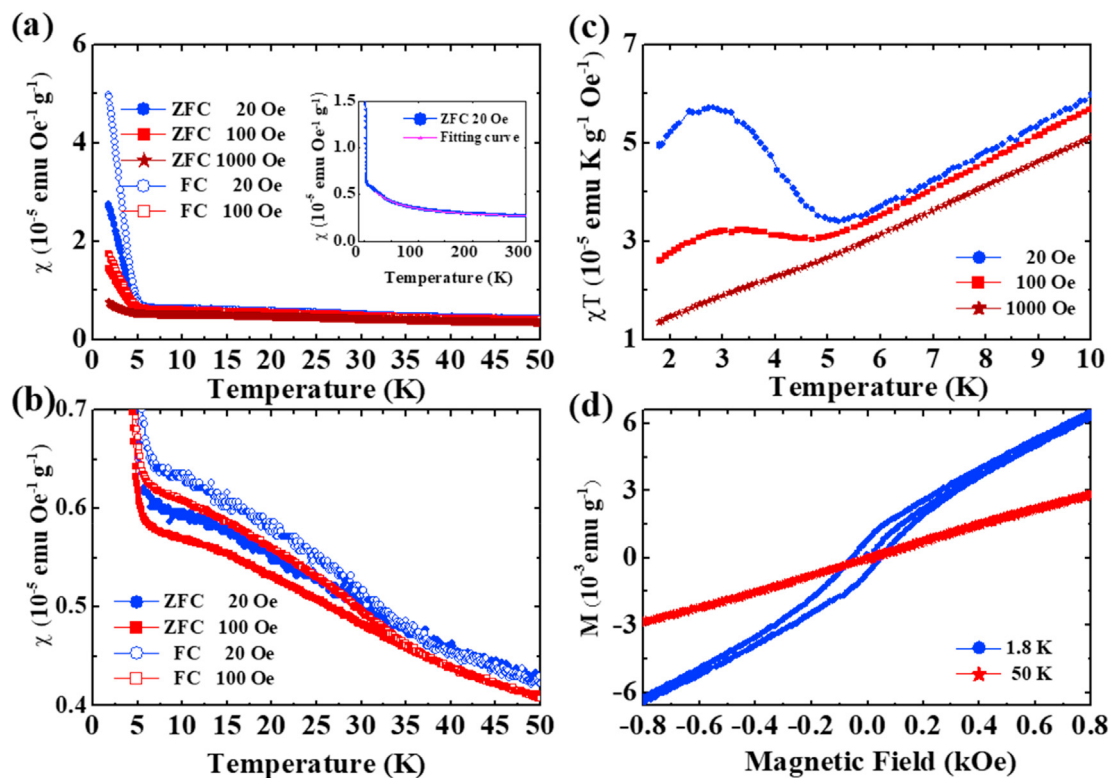
Fig. 1. **(a)** The temperature dependence of the *dc* magnetic susceptibility χ for sample A in the applied magnetic fields of 20, 100, and 1000 Oe with ZFC and FC runs. The inset figure shows ZFC χ at 20 Oe and its fitting curve. **(b)** The magnified FC and ZFC χas a function of temperature at 20 and 100 Oe. **(c)** The temperature dependence of the product of ZFC χ and T at 20, 100, and 1000 Oe. **(d)** The magnetic field dependence of the magnetization M at 1.8 and 50 K. (A colour version of this figure can be viewed online.)

special magnetic hysteresis loop has been observed in the typical weak ferromagnets and attributed to the dominant AFM interaction [34,38]. The weak FM transition at 5.2 K was also demonstrated in three samples labeled as B, C and D (see Figures S2−S4 in the Supplementary Data). In Fig. S4(b), we present the FC magnetic susceptibilities measured by Quantum Design (QD) and our group for Palladium Standard provided by QD. Our measurement for Palladium Standard was performed along with sample D on the same day. One can clearly see that QD and our measurements exhibit a very similar magnetic behavior in the temperature range of 1.8−300 K. This demonstrates that the SQUID magnetometer works normally in our laboratory and the weak FM transition at 5.2 K reflects the intrinsic property of K-intercalated 9-PAN. Herein, we would like to point out that the weak ferromagnetism in K-intercalated 9-PAN is unlikely to be related to defects created in the intercalation process, since the magnetic transition temperature induced by defects usually is above room temperature, and the typical examples include highly oriented pyrolytic graphite [8−11] and ZnO [43,44].

3.2. Crystal and electronic structures of K-intercalated 9-PAN

Fig. 2 displays the XRD patterns of pristine and K-intercalated materials. $K_3$9-PAN-A and $K_3$9-PAN-B in the figure correspond to samples A and B, respectively. Pristine 9-PAN crystallizes in the triclinic space group P1, with two molecules of $C_{20}H_{14}$ in a unit cell of dimensions a = 6.247 Å, b = 10.259 Å, c = 10.779 Å, and V = 654.7 Å³. The two strongest peaks at 8.5° and 16.9° for the pristine material are in good agreement with the ones in the standard powder diffraction file (PDF) card. The rather weak peak at 20.6° compared with the PDF card indicates that purchased 9-PAN has a preferred orientation growth along the [001] direction.

Upon intercalating potassium, three new peaks appear at 7.3°, 9.7°, and 21.9°, which do no match with the peaks in the standard PDF card. A detailed comparison between measured results and the XRD patterns of K and KH indicates that the peaks marked by ◆ and * actually correspond to potassium and KH, respectively. The by-product KH may originate from the reaction of potassium with hydrogen at the active 10-position of anthracene.

To identify the crystal structure of K-intercalated 9-PAN, we inserted potassium atoms into the interstitial space of 9-PAN according to the mole ratios of 1:1 and 2:1 between potassium atoms and 9-PAN molecules, and then performed a full relaxation of atomic positions. The optimized results showed that one crystal structure with a mole ration of 2:1 can reflect the main character of the measured XRD results, and the atomic positions of C, H, and K can be found in the Supplementary Data. In this crystal, two 9-PAN molecules and four K atoms distribute in a unit cell of dimensions a = 7.288 Å, b = 12.851 Å, c = 9.745 Å, α = 82.935°, β = 70.930°, and γ = 66.804°, as shown in Fig. 3a. The powder XRD pattern based on the searched crystal, as indicated by "Calculated" in Fig. 2, is in good agreement with the measured one. The very weak peaks near 15.9° compared with the theoretical modelling are possible due to preferred orientation growth of synthesized materials, similar to the case of purchased 9-PAN.

The green arrows in Fig. 3a stand for the unpaired electron spins on charged phenyls and anthracenes, and the numbers besides the arrows indicate their amplitudes in the unit of μ_B. It is clear to see that the spins on the same 9-PAN molecule tend to align in the same direction, while those on different molecules in the unit cell prefer an antiparallel alignment. Summation of all unpaired spins in the unit cell results in a small but nonzero total spin (0.0018 μ_B), as indicated by the purple arrow. The spin arrangement in Fig. 3a was determined by a comparison of the energies of three typical
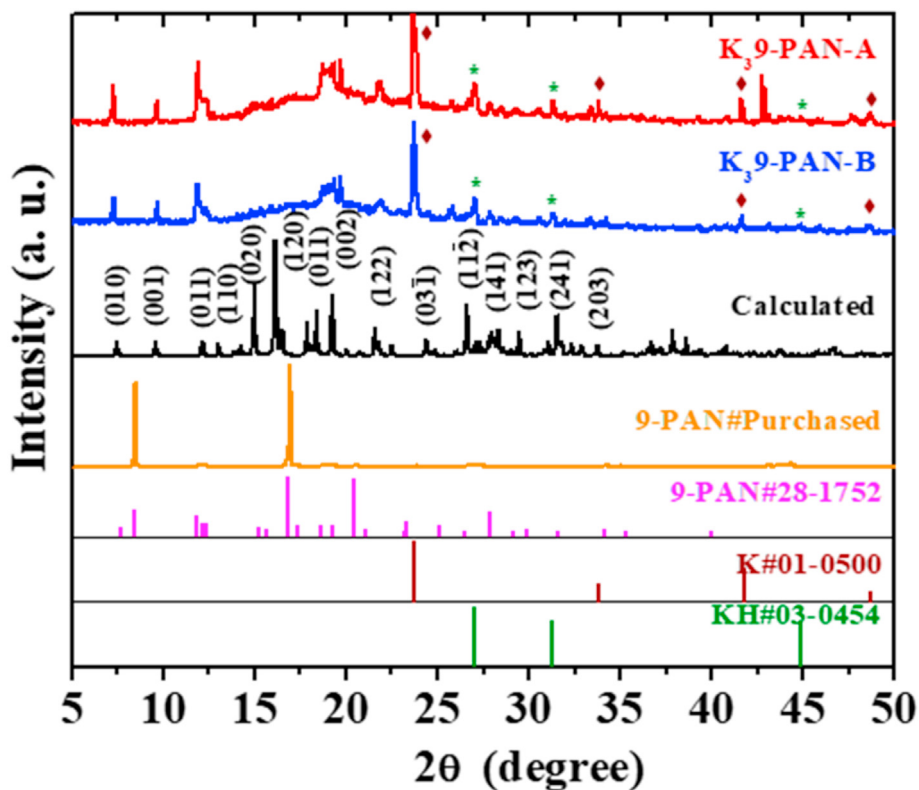
Fig. 2. XRD patterns of pristine and K-intercalated 9-PAN measured at room temperature. In Figs. 2 and 4, 9-PAN, K₃9-PAN-A, and K₃9-PAN-B correspond to pristine 9-phenylanthracene, samples A and B, respectively. The symbols ◆ and * indicate the XRD patterns which match with K and KH. "Calculated" represents the calculated XRD pattern of optimized structure in Fig. 3a. (A colour version of this figure can be viewed online.)

magnetic configurations, i.e., AFM-1 (intramolecular ferromagnetic and intermolecular antiferromagnetic), AFM-2 (intramolecular antiferromagnetic and intermolecular antiferromagnetic) and FM (intramolecular ferromagnetic and intermolecular ferromagnetic) (see Figure S5 in the Supplementary Data). Among the three magnetic configurations, AFM-1 has an energy about 48.6 and 9.0 meV lower than AFM-2 and FM, respectively, indicating that AFM-1 is the magnetic ground state and the intramolecular spin coupling is much stronger than the intermolecular one.

On the basis of theoretical calculations, the results presented in Fig. 1 can be understood as follows. In the paramagnetic regime (above 35 K), the spins within each molecule parallelly align due to the strong intramolecular spin coupling, but no magnetic ordering is formed between molecules. Below 35 K, the AFM ordering between molecules is formed by the intermolecular spin coupling, and the nonzero total spin renders a FM response in the low temperature region. There exist two significant differences from previously reported weak ferromagnets [33—42]. One is that the unpaired electron spins originate from the π-electrons in K-intercalated 9-PAN, while the d-electron or radical is the source of spins in CuF₂(H₂O)₂(pyrazine) [33], [Mn₃{C₆H₃(COO)₃}₂] [34], Fe(pyrimidine)₂Cl₂ [38], sulfur-nitrogen dithiadiazolyl [41], and 2,4,6-triphenylverdazyl [42]. The other one is that the weak ferromagnetism reported before is induced by canting of antiferromagnetically ordered spins with the same amplitude, however, the amplitudes of spins also play a role in forming the weak ferromagnetism in K-intercalated 9-PAN, manifested by the numbers beside the green arrows.

Fig. 3b shows the band structure of K-intercalated 9-PAN, and the corresponding partial density of states (PDOS) and spin-dependent density of states (DOS) are presented in Fig. 3c and d.

One can clearly see that the Fermi level marked by the black dashed line crosses two overlapped bands spanning in a narrow energy region, which are formed from the lowest unoccupied molecular orbital (LUMO) of 9-PAN. The PDOS in Fig. 3c indicate that the states in the vicinity of the Fermi energy are dominated by the C 2p orbital, while the C 2s and K 4s orbitals have a negligible contribution. This result demonstrates that the K 4s electron is transferred to the π-orbital of 9-PAN. The nearly symmetric spin-dependent DOS in Fig. 3d are similar to the characters of conventional antiferromagnet [45], reflecting the fact that spin-up and spin-down unpaired electrons alternatively distribute on the 9-PAN molecules (Fig. 3a). The negative DOS difference between spin-up and spin-down electrons indicates that the down spin has larger DOS than the up spin, leading to a small but nonzero total spin in the unit cell (See Figure S6 in the Supplementary Data). Moreover, the closeness between total and C-2p DOS differences shown in Figure S5 demonstrates that the C 2p orbital is the dominant contribution to the total spin and weak ferromagnetism in K-intercalated 9-PAN.

To exclude the effect of defects on the weak ferromagnetism, we performed a theoretical study of the defect magnetism in K-intercalated 9-PAN. Considering the active 10-position of anthracene and by-product KH in the XRD patterns, the most possible defect in K-intercalated 9-PAN corresponds to carbon dangling bond at the 10-position of anthracene. In our theoretical calculations, we first built two carbon dangling bonds in a $2 \times 2 \times 1$ supercell containing 160 C atoms, 112 H atoms and 16 K atoms, by removing two H atoms at the 10-position of two 9-PAN molecules. Then we computed the total energies for FM and AFM arrangements of two carbon dangling bonds. The obtained results showed that the FM arrangement has an energy about 57 meV lower than the AFM one,
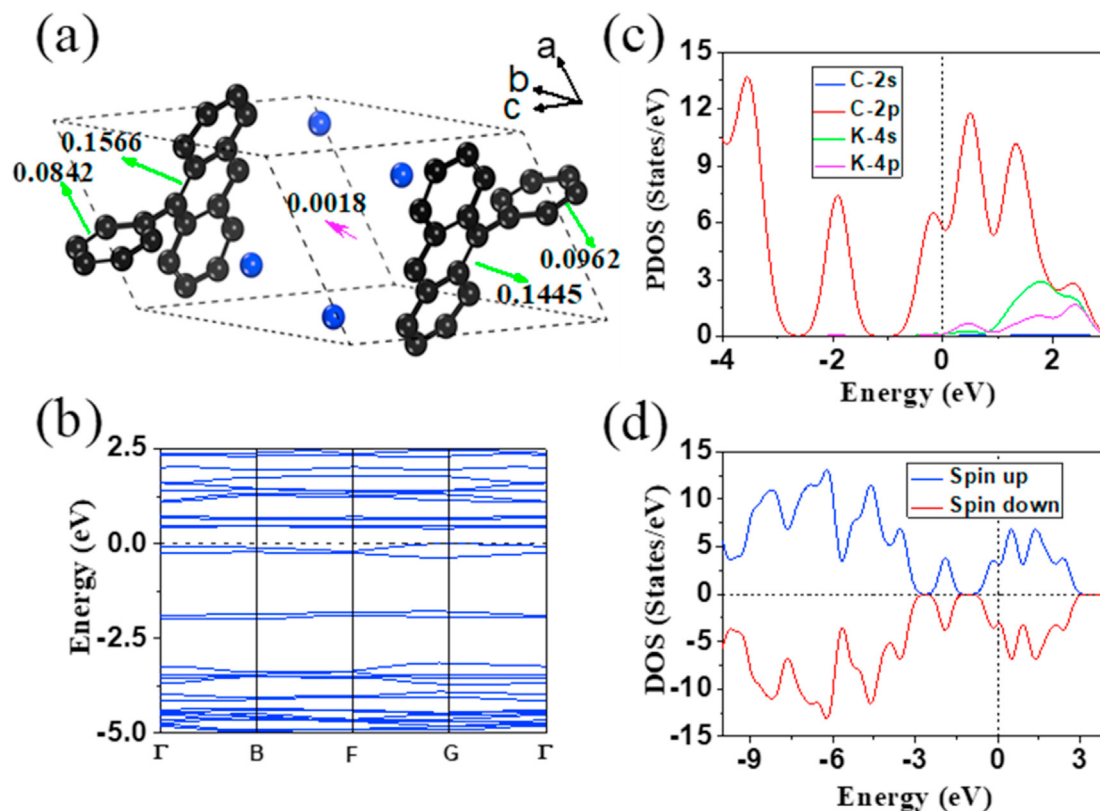
Fig. 3. (a) The arrangement of molecules and potassium in synthesized material is shown in an 1 × 1 × 1 supercell. The black and blue balls represent carbon and potassium atoms, respectively. The hydrogen atoms are not given in the figure for clarity. The green arrows stand for the unpaired electron spins on phenyls and anthracene anions, and the total spin is indicated by the purple arrow. **(c)** The band structure of K-intercalated 9-PAN. **(c)** Orbital-resolved partial density of states (PDOS) as a function of energy. The red, blue, green, and purple solid lines represent PDOS of C-2p, C-2s, K-4s, and K-4p, respectively. **(d)** Spin dependent total density of states (DOS) vs. energy. (A colour version of this figure can be viewed online.)

indicating that two carbon dangling bonds favor a FM ordering at high temperature. Therefore, defects are unlikely to contribute to the weak FM transition at 5.2 K.

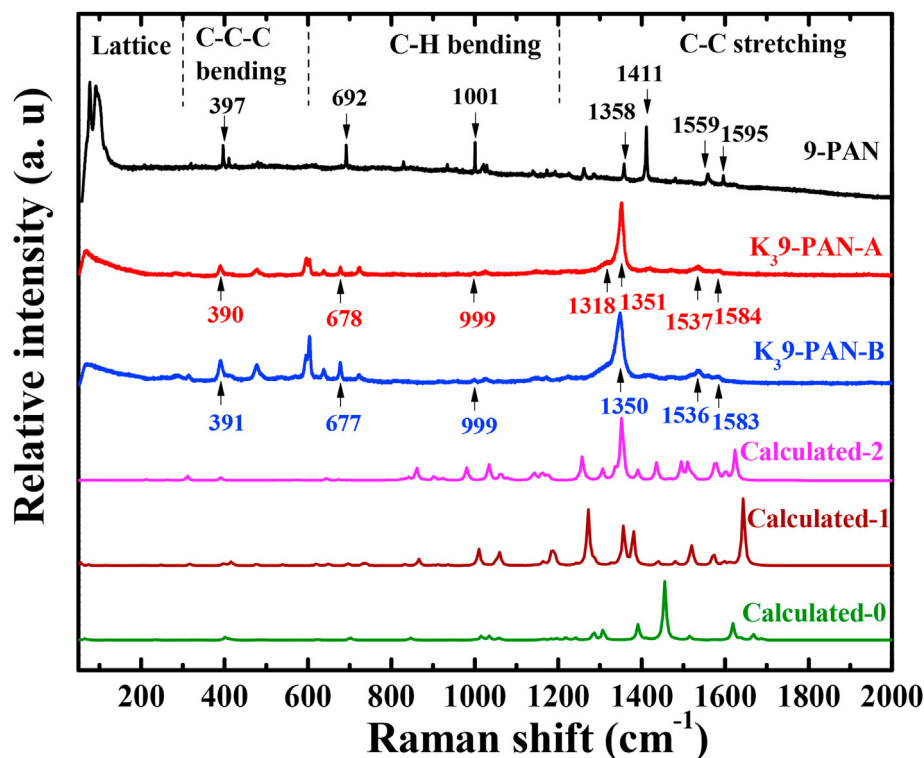### 3.3. Raman spectra of pristine and K-intercalated 9-PAN

The weak FM phase was further characterized by the phase-sensitive Raman spectroscopy. Fig. 4 shows the Raman spectra for pristine and K-doped 9-PAN, as well as the theoretically calculated results for single 9-PAN molecule with zero, one and two charges (scaled by a factor of 0.99). One can readily see that the calculated spectra are in good agreement with the measured ones for pristine 9-PAN, except for a systematic blueshift of calculated peak positions compared with the experimental results. The main character of the spectra for intercalated materials (i.e., one dominant peak at 1351 cm^{-1}) can be qualitatively reflected by the calculated results with two charges. This provides a strong support for the mole ration of 2:1 in K-intercalated 9-PAN.

The Raman active modes of pristine 9-PAN in the frequency range of 50–2000 cm^{-1} can be divided into four regions: lattice, C–C–C bending, C–H bending, and C–C stretching. The mode at 397 cm^{-1} corresponds to the skeletal deformation of anthracene [46]. The two modes at 692 and 1001 cm^{-1} are associated with the C–H bending in the whole molecule and in phenyl, respectively [47]. In the high-frequency region, the two modes at 1358 and 1411 cm-1 involve the C–C stretching and C–H bending in both anthracene and phenyl, while the ones at 1559 and 1595 cm^{-1} correspond to the C–C stretching in anthracene [46] and phenyl [47], respectively. When potassium atoms ate intercalated into 9-

PAN, all lattice modes are strongly suppressed and the seven modes mentioned above shift down by 7, 14, 2, 40, 60, 22, and 11 cm^{-1}, respectively. The redshift phenomenon of Raman modes with potassium intercalating is similar to the situation of K-intercalated picene [48], phenanthrene [49], and triphenylbismuth [50], which has been attributed to the softening effect of transferred electron from metal to organic molecule. Notice that the red shifts for the two modes at 1358 and 1411 cm^{-1} are much larger compared with the other five modes. This difference is understandable in terms of the characters of atomic vibrations. While the atoms in both anthracene and phenyl have equally important contributions to the modes at 1358 and 1411 cm^{-1}, the other five modes are dominated by the atoms in either anthracene or phenyl. As a result, mutual influences of atomic vibrations between anthracene and phenyl, particularly those close to the C–C single bond, produce a stronger softening for the former two modes.

4. Conclusions

The results presented in this paper provide unambiguous evidence for the weak ferromagnetism in K-intercalated 9-PAN. The combination of theoretical calculations and Raman spectra indicates that the magnetism is produced by transferring electron from potassium 4s orbital to carbon 2p orbital on 9-PAN. The unpaired electron spins of phenyl and anthracene anions within the same molecule favor a parallel alignment, while the ones on different molecules in the unit cell prefer an antiparallel alignment, leading to the observed AFM transition at 35 K and weak FM transition at 5.2 K. Similar to other weak ferromagnets containing

Fig. 4. Raman scattering spectra of pristine and K-intercalated 9-PAN collected at room temperature. Four regions of Raman active modes, divided by the vertical dashed lines, are shown above the spectra of pristine material. "Calculated-0/1/2" represents the theoretical result for single 9-PAN molecule with 0, 1, or 2 charges. (A colour version of this figure can be viewed online.)

transition metal atoms or organic radical, canting of antiferromagnetically ordered spins is responsible for the formation of weak ferromagnetism. However, one essential difference from previous reports is that the unpaired electron spins are from the π-electron in K-intercalated 9-PAN, but not from the d-electron of transition metal atom or 2p-electron of radical. This study not only enriches the functionality of 9-PAN but also extends the scope of weak ferromagnets.

CRediT authorship contribution statement

Ming-An Fu: Resources, Data curation. **Ren-Shu Wang:** Data curation. **Hui Yang:** Formal analysis. **Pei-Yuan Zhang:** Resources. **Chun-Fang Zhang:** Formal analysis. **Xiao-Jia Chen:** Supervision. **Yun Gao:** Supervision. **Zhong-Bing Huang:** Conceptualization, Writing - original draft.

Declaration of competing interest

The authors declare that they have no known competing financial interests or personal relationships that could have appeared to influence the work reported in this paper.

Acknowledgment

Appendix A. Supplementary data

Supplementary data to this article can be found online at https://doi.org/10.1016/j.carbon.2020.11.064.

References

[1] J.S. Miller, Magnetically ordered molecule-based materials, Chem. Soc. Rev. 40 (2011) 3266–3296.
[2] P. Bujak, I. Kulszewicz-Bajer, M. Zagorska, V. Maurel, I. Wielgus, A. Pron, Polymers for electronics and spintronics, Chem. Soc. Rev. 42 (2013) 8895–8999.
[3] E.M. Fatila, A.C. Maahs, M.B. Mills, M. Rouzières, D.V. Soldatov, R. Clérac, et al., Ferromagnetic ordering of −[Sm(III)-radical]n− coordination polymers, Chem. Commun. 52 (2016) 5414–5417.
[4] J. Loste, J.M. Lopez-Guesta, L. Billon, H. Garay, M. Save, Transparent polymer nanocomposites: an overview on their synthesis and advanced properties, Prog. Polym. Sci. 89 (2019) 133–158.
[5] G. Mali, M. Mazaj, I. Arčon, D. Hanžel, D. Arčon, Z. Jagličić, Unraveling the arrangement of Al and Fe within the framework explains the magnetism of mixed-metal MIL-100(Al,Fe), J. Phys. Chem. Lett. 10 (2019) 1464–1470.
[6] N.N. Wu, D.M. Xu, Z. Wang, F.L. Wang, J.R. Liu, W. Liu, et al., Achieving superior electromagnetic wave absorbers through the novel metal-organic frameworks derived magnetic porous carbon nanorods, Carbon 145 (2019) 433–444.
[7] R. Dong, Z. Zhang, D.C. Tranca, S. Zhou, M. Wang, P. Adler, et al., A coronene-based semiconducting two-dimensional metal-organic framework with ferromagnetic behaviour, Nat. Commun. 9 (2018) 2637.
[8] P. Esquinazi, A. Setzer, R. Höhne, C. Semmelhack, Y. Kopelevich, D. Spemann, et al., Ferromagnetism in oriented graphite samples, Phys. Rev. B 66 (2002), 024429.
[9] P. Esquinazi, D. Spemann, R. Höhne, A. Setzer, K.-H. Han, T. Butz, Induced magnetic ordering by proton irradiation in graphite, Phys. Rev. Lett. 91 (2003) 227201.
[10] J. Barzola-Quiquia, W. Böhlmann, P. Esquinazi, A. Schadewitz, A. Ballestar, S. Dusari, et al., Enhancement of the ferromagnetic order of graphite after sulphuric acid treatment, Appl. Phys. Lett. 98 (2011) 192511.
[11] X.C. Miao, S. Tongay, A.F. Hebard, Extinction of ferromagnetism in highly ordered pyrolytic graphite by annealing, Carbon 50 (2012) 1614–1618.
[12] K.-H. Han, D. Spemann, R. Höhne, A. Setzer, T. Makarova, P. Esquinazi, et al., Observation of intrinsic magnetic domains in C60 polymer, Carbon 41 (2003)

785—795.

[13] R.A. Wood, M.H. Lewis, M.R. Lees, S.M. Bennington, M.G. Cain, N. Kitamura, Ferromagnetic fullerene, J. Phys. Condens. Matter 14 (2002) L385.

[14] J. Barzola-Quiquia, P. Esquinazi, M. Lindel, D. Spemann, M. Muallem, G.D. Nessim, Magnetic order and superconductivity observed in bundles of double-wall carbon nanotubes, Carbon 88 (2015) 16—25.

[15] A.L. Friedman, H. Chun, Y.J. Jung, D. Heiman, E.R. Glaser, L. Menon, Possible room-temperature ferromagnetism in hydrogenated carbon nanotubes, Phys. Rev. B 81 (2010) 115461.

[16] G.Z. Magda, X. Jin, I. Hagymási, P. Vancsó, Z. Osváth, P. Nemes-Incze, et al., Room-temperature magnetic order on zigzag edges of narrow graphene nanoribbons, Nature 514 (2014) 608—611.

[17] A. Rajca, S. Rajca, Intramolecular antiferromagnetic vs ferromagnetic spin coupling through the biphenyl unit, J. Am. Chem. Soc. 118 (1996) 8121—8126.

[18] E.A. Mostovich, Y. Borozdina, V. Enkelmann, K. Remović-Langer, B. Wolf, M. Lang, et al., Planar biphenyl-bridged biradicals as building blocks for the design of quantum magnets, Cryst. Growth Des. 12 (2012) 54—59.

[19] K. Miyajima, A. Nakajima, S. Yabushita, M.B. Knickelbein, K. Kaya, Ferromagnetism in one-dimensional vanadium—benzene sandwich clusters, J. Am. Chem. Soc. 126 (2004) 13202—13203.

[20] X.L. Wu, R.S. Wang, J. Cheng, G.H. Zhong, X.J. Chen, Y. Gao, et al., Room temperature ferromagnetism in naphthalene, Carbon 136 (2018) 125—129.

[21] J. Vergés, G. Chiappe, E. Louis, L. Pastor-Abia, E. SanFabián, Magnetic molecules created by hydrogenation of polycyclic aromatic hydrocarbons, Phys. Rev. B 79 (2009) 094403.

[22] H. Yang, Z.B. Huang, Y. Gao, Q.H. Lin, Room temperature multiferroicity in hydrogenated triapentafulvalene and pentaheptafulvalene oligomers, J. Chem. Phys. 146 (2017) 084306.

[23] Y. Takabayashi, M. Menelaou, H. Tamura, N. Takemori, T. Koretsune, A. Štefančič, et al., π-electron $S = \frac{1}{2}$ quantum spin-liquid state in an ionic polyaromatic hydrocarbon, Nat. Chem. 9 (2017) 635—643.

[24] A. Štefančič, G. Klupp, T. Knaflič, D.S. Yufit, G.P. Tavčar, A. Potočnik, et al., Triphenylide-based molecular solid—a new candidate for a quantum spin-liquid compound, J. Phys. Chem. C 121 (2017) 14864—14871.

[25] S.N. Spisak, A.Y. Rogachev, A.V. Zabula, A.S. Filatov, R. Clérac, M.A. Petrukhina, Tuning the separation and coupling of corannulene trianion-radicals through sizable alkali metal belts, Chem. Sci. 8 (2017) 3137—3145.

[26] M. Chen, L. Yan, Y. Zhao, I. Murtaza, H. Meng, W. Huang, Anthracene-based semiconductors for organic field-effect transistors, J. Mater. Chem. C 6 (2018) 7416—7444.

[27] T.M. Figueira-Duarte, K. Müllen, Pyrene-based materials for organic electronics, Chem. Rev. 111 (2011) 7260—7314.

[28] G. Kresse, J. Hafner, Ab initio molecular dynamics for liquid metals, Phys. Rev. B 47 (1993) 558—561 (R).

[29] G. Kresse, J. Furthmüller, Efficient iterative schemes for ab initio total-energy calculations using a plane-wave basis set, Phys. Rev. B 54 (1996) 11169—11186.

[30] J.P. Perdew, K. Burke, M. Ernzerhof, Generalized gradient approximation made simple, Phys. Rev. Lett. 77 (1996) 3865—3868.

[31] P.E. Blöchl, Projector augmented-wave method, Phys. Rev. B 50 (1994) 17953—17979.

[32] M.J. Frisch, G.W. Trucks, H.B. Schlegel, G.E. Scuseria, M.A. Robb, J.R. Cheeseman, et al., Gaussian 09, Revision D.01, Gaussian, Inc., 2013. Wallingford, CT.

[33] J.L. Manson, M.M. Conner, J.A. Schlueter, A.C. McConnell, H.I. Southerland, I. Malfant, et al., Experimental and theoretical characterization of the magnetic properties of $CuF_2(H_2O)_2$(pyz) (pyz = pyrazine): a two-dimensional quantum magnet arising from supersuperexchange interactions through hydrogen bonded paths, Chem. Mater. 20 (2008) 7408—7416.

[34] P. Mahata, D. Sen, S. Natarajan, A three-dimensional metal—organic framework with a distorted Kagome related layer showing canted antiferromagnetic behaviour, Chem. Commun. (2008) 1278—1280.

[35] J.R. Li, Q. Yu, Y. Tao, X.H. Bu, J. Ribas, S.R. Batten, Magnetic canting or not? Two isomorphous 3D CoII and NiII coordination polymers with the rare non-interpenetrated (10, 3)-d topological network, showing spin-canted antiferromagnetism only in the CoII system, Chem. Commun. (2007) 2290—2292.

[36] K.C. Mondal, G.E. Kostakis, Y. Lan, C.E. Anson, A.K. Powell, Spin-canting and metamagnetic behavior in a new species from the hydrothermal Co(II)-trans-3-pyridylacrylate system, Inorg. Chem. 48 (2009) 9205—9213.

[37] M.H. Zeng, W.X. Zhang, X.Z. Sun, X.M. Chen, Spin canting and metamagnetism in a 3D homometallic molecular material constructed by interpenetration of two kinds of cobalt(II)-coordination-polymer sheets, Angew. Chem. Int. Ed. 44 (2005) 3079—3082.

[38] R. Feyerherm, A. Loose, T. Ishida, T. Nogami, J. Kreitlow, D. Baabe, et al., Weak ferromagnetism with very large canting in a chiral lattice: Fe (pyrimidine)$_2$Cl$_2$, Phys. Rev. B 69 (2004) 134427.

[39] L. Arai, M.A. Nadeem, M. Bhadbhade, J.A. Stride, A 2D cobalt based coordination polymer constructed from benzimidazole and acetate ion exhibiting spin-canted antiferromagnetism, Dalton Trans. 39 (2010) 3372—3374.

[40] V.E. Dmitrienko, E.N. Ovchinnikova, S.P. Collins, G. Nisbet, G. Beutier, Y.O. Kvashnin, et al., Measuring the Dzyaloshinskii—Moriya interaction in a weak ferromagnet, Nat. Phys. 10 (2014) 202—206.

[41] A.J. Banister, N. Bricklebank, I. Lavender, J.M. Rawson, C.I. Gregory, B.K. Tanner, et al., Spontaneous magnetization in a sulfur—nitrogen radical at 36 K, Angew. Chem. Int. Ed. 35 (1996) 2533—2535.

[42] S. Tomiyoshi, T. Yano, N. Azuma, M. Shoga, K. Yamada, J. Yamauchi, Weak ferromagnetism and antiferromagnetic ordering of 2p electrons in the organic radical compound 2, 4, 6-triphenylverdazyl, Phys. Rev. B 49 (1994) 16031—16034.

[43] G.Z. Xing, Y.H. Lu, Y.F. Tian, J.B. Yi, C.C. Lim, Y.F. Li, et al., Defect-induced magnetism in undoped wide band gap oxides: zinc vacancies in ZnO as an example, AIP Adv. 1 (2011), 022152.

[44] L.N. Mahour, H.K. Choudhary, R. Kumar, A.V. Anupama, B. Sahoo, Structural, optical and Mossbauer spectroscopic investigations on the environment of Fe in Fe-doped ZnO (Zn1-xFexO) ceramics synthesized by solution combustion method, Ceram. Int. 45 (2019) 24625—24634.

[45] K.L. Yao, X.L. Li, Z.L. Liu, Y.L. Li, G.Y. Gao, First-principles study on the metallic antiferromagnet Co[PhPO$_3$]·H$_2$O, J. Magn. Magn Mater. 312 (2007) 16—20.

[46] Y. Xie, X. Wang, X. Han, X. Xue, W. Ji, Z. Qi, et al., Sensing of polycyclic aromatic hydrocarbons with cyclodextrin inclusion complexes on silver nanoparticles by surface-enhanced Raman scattering, Analyst 135 (2010) 1389—1394.

[47] A. Łapiński, J. Spanget-Larsen, M. Langgård, J. Waluk, J.G. Radziszewski, Raman spectrum of the phenyl radical, J. Phys. Chem. 105 (2001) 10520—10524.

[48] T. Kambe, X. He, Y. Takahashi, Y. Yamanari, K. Teranishi, H. Mitamura, et al., Synthesis and physical properties of metal-doped picene solids, Phys. Rev. B 86 (2012) 214507.

[49] X.F. Wang, R.H. Liu, Z. Gui, Y.L. Xie, Y.J. Yan, J.J. Ying, et al., Superconductivity at 5 K in alkali-metal-doped phenanthrene, Nat. Commun. 2 (2011) 507.

[50] R.S. Wang, J. Cheng, X.L. Wu, H. Yang, X.J. Chen, Y. Gao, et al., Superconductivity at 3.5 K and/or 7.2 K in potassium-doped triphenylbismuth, J. Chem. Phys. 149 (2018) 144502.